Experimental and numerical investigation of the shear behaviour of infiltrated woven fabrics

Christian Poppe[a,*], Dominik Dörr[a], Frank Henning[a,b], Luise Kärger[a]

[a] Karlsruhe Institute of Technology, Institute for Vehicle System Technology, Chair of Light-Weight Technology, Rintheimer Querallee 2, 76131 Karlsruhe, Germany
[b] Fraunhofer Institute for Chemical Technology, Polymer Engineering Department, Joseph-von-Fraunhofer-Str. 7, 76327 Pfinztal, Germany

Keywords:
Textile characterisation
Forming
Wet compression moulding (WCM)
Process simulation
Finite Element Method (FEM)

A B S T R A C T

Wet compression moulding (WCM) as a promising alternative to resin transfer moulding (RTM) provides high-volume production potential for continuously fibre reinforced composite components. Lower cycle times are possible due to the parallelisation of the process steps draping, infiltration and curing during moulding. Although experimental and theoretical investigations indicate a strong mutual dependency arising from this parallelisation, no material characterisation set-ups for textiles infiltrated with low viscous fluids are yet available, which limits a physical-based process understanding and prevents the development of proper simulation tools. Therefore, a modified bias-extension test set-up is presented, which enables infiltrated shear characterisation of engineering textiles. Experimental studies on an infiltrated woven fabric reveal both, rate- and viscosity-dependent shear behaviour. The process relevance is evaluated on part level within a numerical study by means of FE-forming simulation. Results reveal a significant impact on the global and local shear angle distribution, especially during forming.

1. Introduction

Wet compression moulding (WCM) provides high volume production potential for continuously fibre reinforced components as a promising alternative to resin transfer moulding (RTM). The simultaneous draping, infiltration and curing (viscous draping) enables reduced cycle times. Experimental and theoretical investigations indicate strong mutual dependencies between the key process parameters, such as resin amount and resin application position/technique, infiltration time, tool settings (closing profile, temperature, pressure) and stack weight [1–3]. Beyond that, an influence of resin amount and infiltration time on the structural performance is observed by Heudorfer et al. [4].

Despite that, there is hardly any literature available, which investigates the cause of these mutual dependencies. This includes the impact of infiltration on the draping behaviour, as well as the effect of higher fluid pressures superimposed to the forces during draping. This impedes a comprehensive and physical based understanding of the above outlined interactions and thus limits the development of reasonable process simulation methods for the WCM process [1,5].

The investigated thermoset based WCM process consists of five process steps simular to the process investigated by Bergmann et al. [1,2] (cf. Fig. 1). After the laminate is cut and stacked (1), the topside of the stacked laminate is impregnated with resin using a wide slot nozzle (2). While the resin slowly seeps into the laminate, the partially impregnated stack is transferred to the mould (3). The stack is simultaneously draped and fully impregnated within the next process step (4), which is called viscous draping. The part can be demoulded when shape stability is reached, which is determined by the curing velocity of the resin (5). Since significant cavity pressures develop only towards the end of the tool stroke, the influence of resin on the draping is mainly limited to the intra ply and interface behaviour. Therefore, the investigation of infiltrated material behaviour provides important information to understand and model the mutual dependencies between the process parameters within the WCM process. To the author's knowledge, no test benches for the characterisation of infiltrated engineering fabrics are available yet, although research in the field of prepreg thermosets and thermoplastic UD tapes revealed strong dependencies between the matrix material state (viscosity) and mechanical properties during shear [6,7] or bending [8] deformation.

In the first part of this study, a modified version of the bias extension test (IBET: Infiltrated bias extension test), which enables infiltrated shear characterisation of unidirectional or woven/bidirectional reinforced textiles, is presented (Section 2) and validated (Section 3), since in plane shear provides the main deformation mechanism of engineering textiles during draping [7]. For characterisation of the shear behaviour of dry woven and non crimed fabrics (UD NCF), the bias

* Corresponding author.
E-mail address: christian.poppe@kit.edu (C. Poppe).

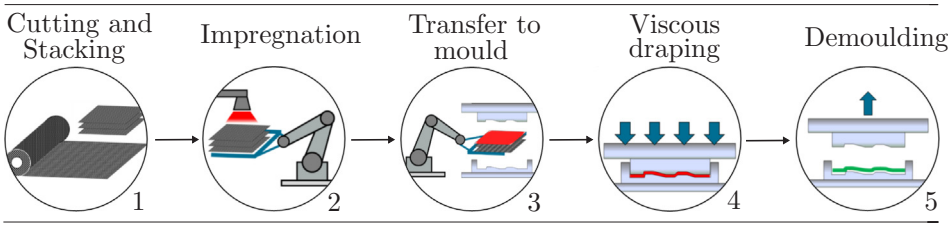

Fig. 1. Schematic illustration of the principle WCM process steps. (For interpretation of the references to color in this figure legend, the reader is referred to the web version of this article.)

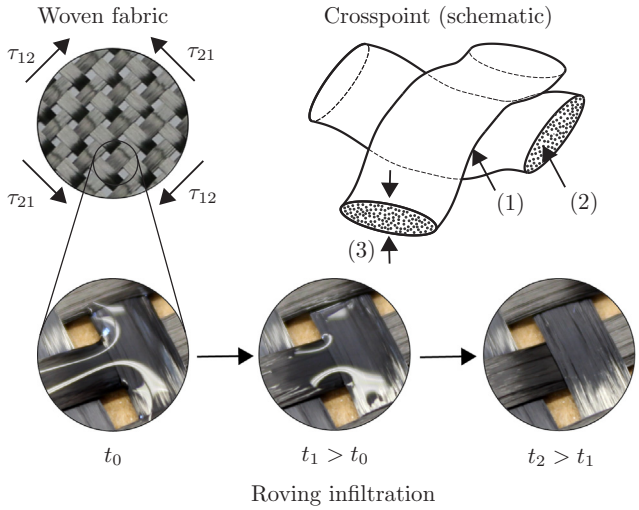

Fig. 2. Illustration of the expected infiltration mechanisms: Change of friction at crosspoints (1), change of internal friction and bending behaviour (2), as well as change of compaction behaviour due to infiltration of the rovings (3); bottom: A visualisation of the impregnation process (t_0–t_2) at a crosspoint and into the roving. (For interpretation of the references to color in this figure legend, the reader is referred to the web version of this article.)

extension tests (BET) [7,9,10] or picture frame tests (PF) [9,11 13] are usually applied. Both tests provide their own advantages and dis advantages [10,14]. While the BET provides a quite simple and fast characterisation approach, several authors observed drawbacks in terms of mesoscopic effects (inter tow slip, crossover slip, fibre bending) during the characterisation of dry fabrics [14 16]. On the contrary, the deformation modes shear and tension can be decoupled using PF tests, which enables the investigation of shear tension coupling for woven fabrics, except for UD NCFs [10]. However, miss alignment and in plane bending of the fibers can provide challenges when using the PF test [12,17 19]. The modified design is based on a BET set up, rather than a PF, since its enables shear characterisation for a wider range of textiles, including unidirectional non crimp infiltrated fabrics [10]. Additional picture frame tests and optical evaluations are per formed to estimate and evaluate the impact of mesoscopic effects on the predictive accuracy of the locking angle.

In the second part of this study (Section 4) FE forming simulation is used to access the process relevance of infiltration dependent shear behaviour on part level. FE forming simulation is used, since it enables a detailed analysis of the resulting deformation by means of constitutive modelling of the material behaviour, considering process and boundary conditions [20 22]. Representation of forming behaviour is based on constitutive modelling of the relevant deformation mechanisms, which are usually separated into intra ply mechanisms for the single plies (membrane and bending) and interface mechanisms (friction and ad hesion) [20,23]. On a macroscopic scale, membrane and bending be haviour have to be decoupled, since in plane fibre tensile stiffness is several decades higher than the bending stiffness [8,24]. This is often achieved by stacking of membrane and shell elements or by an internal physical decoupling within one element [22].

In this study, a macroscopic FE forming simulation approach is used, including a hyperviscoelastic membrane model, which is para metrised with the results of the infiltrated shear characterisation (Section 4.2). The membrane model is implemented by means of in variants, similar to the approaches presented by [25 27] within a material subroutine (VUMAT) in the commercially available FE solver Abaqus. A nonlinear shear modulus, depending on shear angle and shear rate analogue to the approach presented by Machado et al. [6] is used. Straightening of the fibers is taken into account, since it is re quired for a correct parametrisation with the BET set up [28]. However, a direct implementation of a tension shear coupling, as among others proposed by Komeili et al. [29], is neglected since the modified IBET does not provide the possibility to measure this mechanism yet. To account for bending behaviour, a hypoelastic non orthogonal material model, implemented via a user subroutine (VUGENS) in Abaqus by Dörr et al. [8], is used within a superimposed shell element.

2. Characterisation set-up for infiltrated shear behaviour

2.1. Requirements and infiltration mechanisms

Beyond dry textile shear characterisation, the new set up is designed to allow the investigation of a wide range of fully infiltrated textiles, including fluids with low viscosity (≈20 mPa s). The use of pre in filtrated specimens within a common vertical BET reveals several drawbacks. On the one hand, a homogeneous infiltration state, espe cially for lower viscosities, cannot be guaranteed during testing, since resin constantly seeps downwards due to the gravity. Beyond that, the residual weight of the resin overlays the measured force response. On the other hand, it is expected that the fluid within the rovings and around the crosspoints contributes to the shear resistance, especially for higher viscosities and shear rates. This mechanism could be influenced by the absence of fluid around the sample. A reproducible and homo geneous infiltration state of the specimens during testing is anticipated to be of high importance, because of three main infiltration mechanisms that are expected to have an impact on the measured shear behaviour response (cf. Fig. 2(1 3)). Preliminary investigations show, that the resin seeps into the rovings and thickens them, which is expected to influence shear behaviour due to a change in bending stiffness (1) as well as in compaction behaviour (3) of the rovings. Furthermore, resin could form a lubrication layer at the crosspoints of the rovings, which changes frictional behaviour (2), depending on fluid viscosity and possibly slip rate. All of these mechanisms significantly depend on a homogeneous infiltration state of the specimens. Hence, to ensure a homogeneous infiltration state during testing, the characterisation set up should provide shear testing in a fluid reservoir. This makes a hor izontal alignment reasonable.

2.2. Design of the modified infiltrated bias extension test (IBET)

The IBET is designed as a horizontal bias extension test within an additional fluid reservoir (cf. Fig. 3). As shown in Fig. 3(b), the rear fixture remains fixed during the test, while the front fixture is pulled by a steel rope with a low bending stiffness, which is mounted on a load cell of a tensile testing machine. To ensure a reproducible initial posi tioning and to prevent initial deformation of the specimen, the

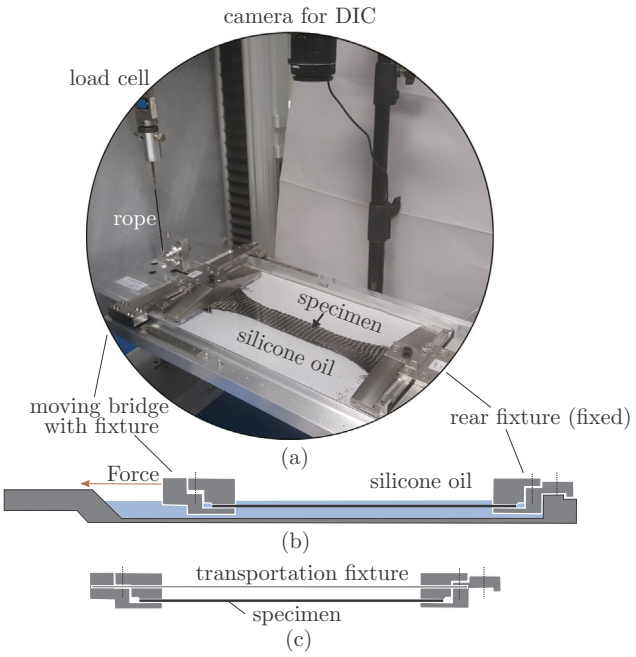

Fig. 3. Design of the modified test beach (IBET); (a) Picture of complete set-up within a tensile testing machine; (b) schematic vertical section view; (c) transfer configuration. (For interpretation of the references to color in this figure legend, the reader is referred to the web version of this article.)

specimens are positioned and clamped on an additional preparation table outside the fluid reservoir. The IBET design allows the removal of the inner fixture, including the undeformed sample from the rest of the test bench, by the use of additional transportation fixtures as illustrated in Fig. 3(c). This enables the transfer of the undeformed sample from the preparation table to the infiltrated test position. The specimen fixture is designed to enable high normal forces to ensure clamping of the specimen even within the fluid environment. An additional layer of thin rubber is used to distribute normal forces and to raise friction within the fixture. Additional heater units can be used to heat the fluid reservoir.

2.3. Evaluation methodology

Due to the horizontal design, additional forces are superimposed to the shear resistance of the specimens. This includes frictional forces within the linear bearings (F_{fric}), which are determined using calibration tests without specimens. Furthermore, fluid resistance is taken into account for impregnated tests as a function of viscosity and velocity ($F_{\text{fluid}}(\eta, v)$), determined by additional calibration test. Additionally, compliance of the steel rope is taken into account. Hence, the resulting forces (F_{result}) are calculated from the raw signal (F_{raw}) by

$$F_{\text{result}} = F_{\text{raw}} - F_{\text{fric}} - F_{\text{fluid}}(\eta, v), \tag{1}$$

where $F_{\text{fluid}}(\eta, v)$ has not to be considered for dry tests. All calibration tests are conducted 10 times.

The real shear angle within the mid segment and the outer shape of the specimens are measured with an optical system during all tests. This includes a camera system with a downstream in house DIC Tool based on an enhancement of an open source matlab script [30]. A pattern is applied to each specimen, which is detected and tracked by the DIC Algorithm. All shown results are based on the optically measured angle within the mid segment.

2.4. Validation

For the validation of the IBET, dry sample results are compared to a conventional BET. The same material as presented in Section 3.1 is used. It is observed that the results are in good agreement (cf. Fig. 4). However, standard deviation for the IBET is slightly increased, especially for low shear angles and forces, due to the uncertainties within the forces determined by Eq. (1). Moreover, gravity leads to some sag of the dry specimens (≈ 1 cm), which does not measurably influences the results. Besides that, sag vanishes in infiltrated tests. Hence, the horizontal IBET design provides comparable results to the BET and can therefore be applied for the shear characterisation of infiltrated woven fabrics.

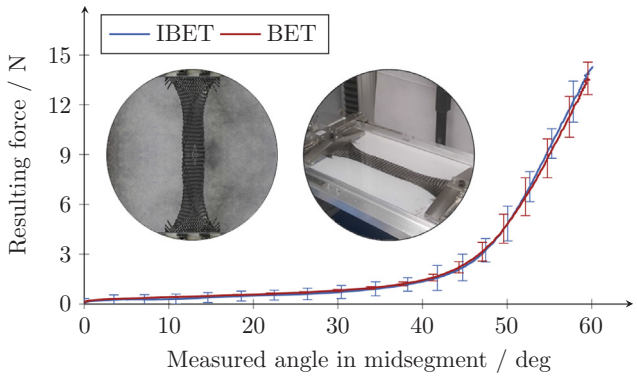

Fig. 4. Validation result for dry specimens using a conventional BET and the modified IBET. (For interpretation of the references to color in this figure legend, the reader is referred to the web version of this article.)

3. Experimental investigations

3.1. Material, equipment, procedure and parameter space

In this study a sigmatex (GB) 12 K carbon plain weave woven fabric without tackifier is used. It is made of T700SC 12K 50C Zoltek fibers. The area weight is 330 ± (10) g/m^2 and roving width is 5.0 ± 0.5 mm, while the initial spacing measures 2.0 ± 0.3 mm. A Inspekt 50 static tensile testing machine (Hegewald & Peschke, Nossen, Germany) in combination with a 100 N load cell is used to record the force displacement curves during testing. Silicone oils (Quax GmbH, Otzberg, Germany) with three different viscosities (20, 135 and 250 ± 3 mPa s) are used as test fluids to avoid additional uncertainties due to the temperature field. Rheometer tests showed no rate dependency of the viscosity within a shear rate range of 1 1000 s^{-1}. The investigated viscosities are chosen based on the process limits. The lowest possible process viscosities are between 10 and 30 mPas and the highest expected viscosities are determined by the gel point of the applied resin (200 250 mPas). Since rate dependency of the infiltrated material is expected, three different velocities 100, 350 and 700 mm/min are investigated. To ensure a complete and homogeneous infiltration, the specimens remain within the fluid for two minutes prior to the testing. Five to eight specimens are tested for every configuration, depending on the actual scatter.

Beyond that, additional uni axial tests with dry samples (280 × 120 mm) within a BET set up are conducted to parametrise the elongation behaviour in fibre direction, which is needed for parametrisation of the numerical model in Section 4. Experimental results in conjunction with the model parametrisation are presented in Section 4.2.

3.2. Mesoscopic effects during BET and its influence on the locking angle

The investigations in this study reveal mesoscopic effects consistent with the literature [7], which includes relative slip of fibers and fibre bending. Similar to the findings of Harrison et al. [14], crossover and inter tow slip occur during higher shear angle within the zone C (cf.

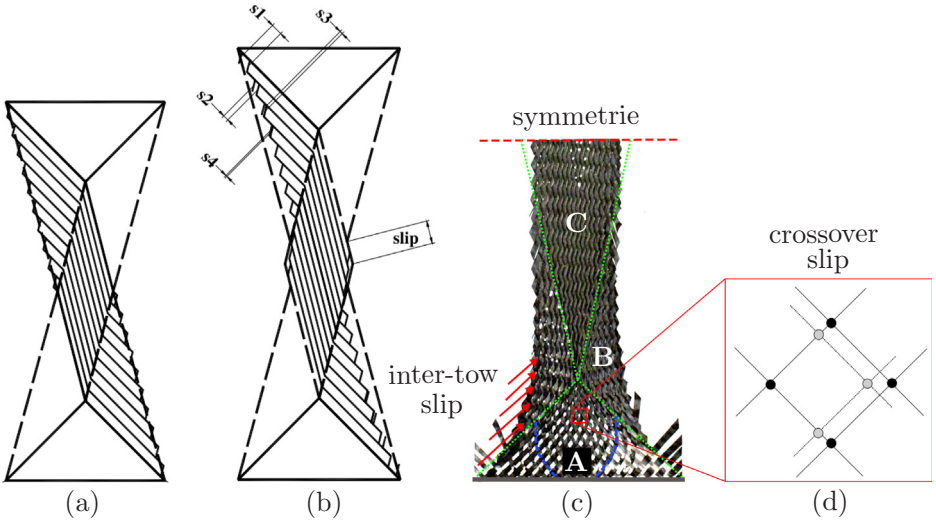

Fig. 5. Comparison of mesoscopic effects during BET/IBET in literature and experiment; (a, b) Schematic illustration of the inter-tow slip mechanism [14], (c) Picture of a tested sample in final deformation state, (d) schematic illustration of the crossover slip mechanism [14]. (For interpretation of the references to color in this figure legend, the reader is referred to the web version of this article.)

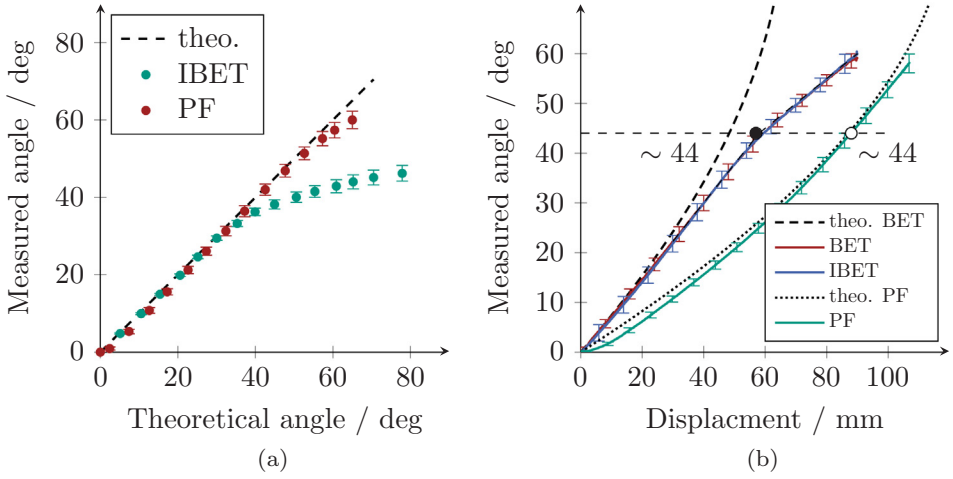

Fig. 6. (a) Comparison of measured vs. theoretical shear angle; (b) comparative determination of the locking angle by means of angle-displacement curves of dry woven fabrics. (For interpretation of the references to color in this figure legend, the reader is referred to the web version of this article.)

Fig. 5). However, a comparison of the final deformation states did not indicate any connection between the occurrence of the slipping effects or the slip distance within the specimens and its infiltration state. Ra ther identical local slip is found in all specimens, leading to one re presentative curve for the outer shape of the textiles (cf. Fig. 13). Be yond that, in plane bending of the fibers and rovings can be found, as observed by Bel et al. [16] (cf. Fig. 5(c, blue dashed lines)). The optical detection method used to measure the shear angle of specimens could also confirm the three stages of dominant mechanisms during BETs (1. shear, 2. tension, 3. slippage) as presented by Zhu et al. [15].

According to Harrison et al. [14], the BET is able to predict the material locking angle correct, despite the occurring mesoscopic effects. To clarify whether this predicate holds true for the used material within the IBET set up, additional PF tests with dry specimens are conducted. The comparison of the measured and theoretical shear angles for the tests provide results similar to the findings of Harrison et al. [14] (cf. Fig. 6(a)). The measured angle curve of the IBET deviates from the theoretical one only above 39 degrees. These results indicate, that the mesoscopic effects do not measurably influence the material response, or do not significantly occur during the IBET for shear angles below 39 degrees. However, this does not indicate whether the material locking angle can be predicted correctly.

Regarding the prediction and determination of the material locking angle, two distinct definitions based on the displacement and measured angle curves for the PF and IBET are used due to the different kinematic and boundary constitutions within both tests. This provides the ad vantage that only kinematic information are used and no normalisation is needed. The material locking angle of the IBET and BET is determined as the point at which the tangents of the transition and locking regions intersect (cf. Fig. 6(b, black filled dot)). This marks the point, where tensioned fibers in zone C have fully closed the gaps between the rov ings and get into contact with each other. Further shear deformation due compaction of the rovings is possible, thus the angle still increases. However, higher tensions in zone C also lead to mesoscopic slip, as outlined above. Regarding the PF, the material locking angle can be identified as the turning point at which the measured angle within the specimen does not longer tend towards the theoretical curve (cf. Fig. 6(b, white filled dot)). At this stage the material locking leads to increased shear resistance of the specimens.

The comparison of the results of the additional PF tests with the BET/IBET reveal a minor influence of the mesoscopic effects during angles below the locking angle (44 ± 2 deg). However, it can be confirmed that at a certain point (30 44 deg), which depends on the fabric's geometrical architecture, mesoscopic effects start to alter the measured force response of the fabric during BETs, indicated the de viation between the theoretical and measured curves. Beyond that, the locking angle can be predicted correctly for the used material by means of IBETs. The results of Harrison et al. [14] could be confirmed for the investigated material.

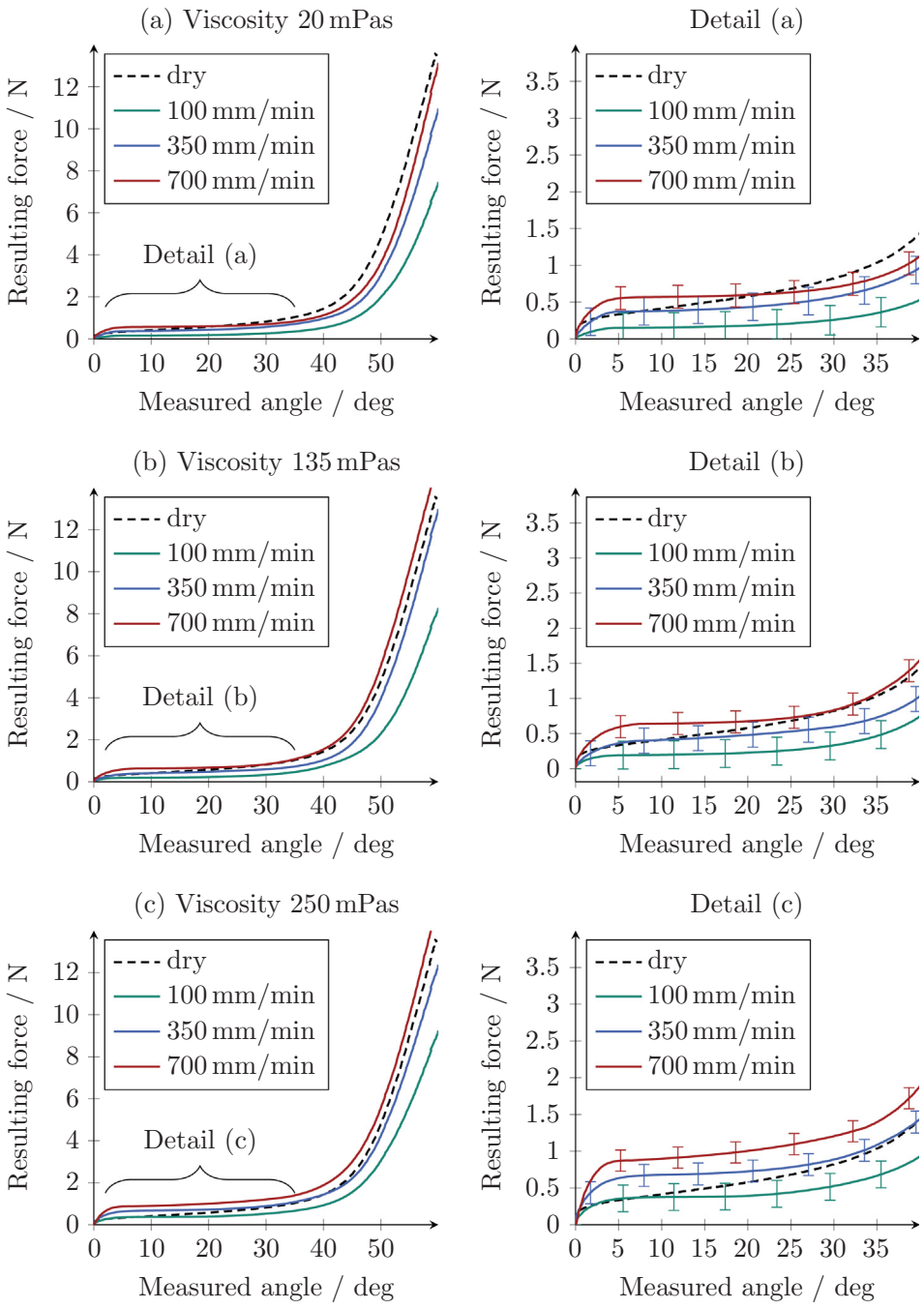

Fig. 7. Experimental results for dry and infiltrated specimens; left: complete range; right: detailed view on the 0–40 deg shear angle range. (For interpretation of the references to color in this figure legend, the reader is referred to the web version of this article.)

3.3. Experimental results

The experimental results are shown in Fig. 7(a c), including addi tional detailed views on the region 0 40 deg. The resulting curves of the dry specimens can be used as a reference line, since the dry results are found to be rate independent at room temperature. A viscosity de pendency is observable by means of an offset between results with the same deformation rate and varying viscosity (cf. Fig. 8). Beyond that, a rate dependency is observed by means of increasing shear force re sponse for higher test velocities. Furthermore, the locking angle is ob served to be shifted towards lower shear angles with increasing shear rate. This can be exemplified by the 250 mPa s fluid results, where the locking angle decreases from 48 to 43 degrees ($\gamma_{lock}^{(100)} = 48$ deg, $\gamma_{lock}^{(350)} = 46$ deg, $\gamma_{lock}^{(700)} = 43$ deg).

Moreover, the curve characteristics of the infiltrated specimens are found to be differing from the dry ones (cf. Fig. 7 (detail (a)). While the dry curves increase rather monotonous until the locking region is reached, the infiltrated curves remain constant or show a far less in crease.

It can be observed that a low viscosity (20 mPa s) reduces the shear resistance of the fabric compared to the dry specimens, especially in combination with low deformation rates (cf. Fig. 8). On the contrary, a high viscosity (250 mPa s) leads to an increased shear resistance com pared to the dry specimens, for example when comparing the relative positions of the viscous curves to the dry curves in detail (a) to (c). Additionally, rate dependency increases with increasing viscosity, as the offset between the infiltrated curves increase from (a) to (c).

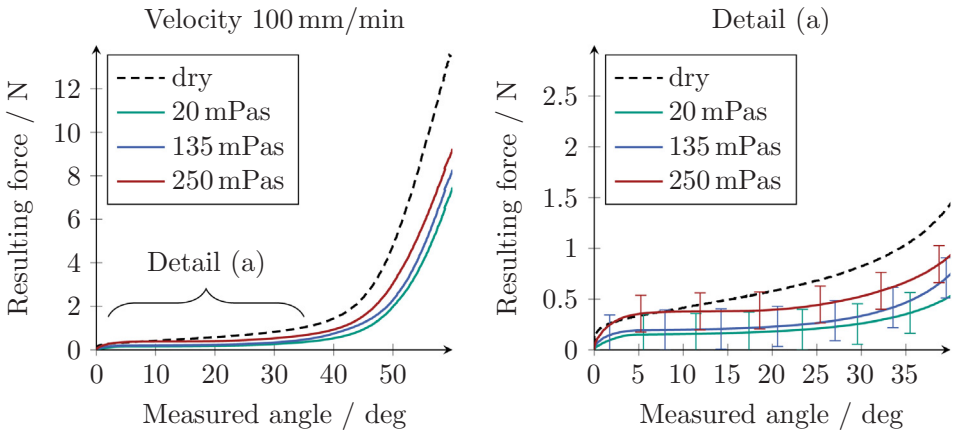

Fig. 8. Visualisation of the effect of viscosity at a constant rate of 100 mm/min for dry and infiltrated specimens; left: complete range; right: detailed view on the 0–40 deg shear angle range. (For interpretation of the references to color in this figure legend, the reader is referred to the web version of this article.)

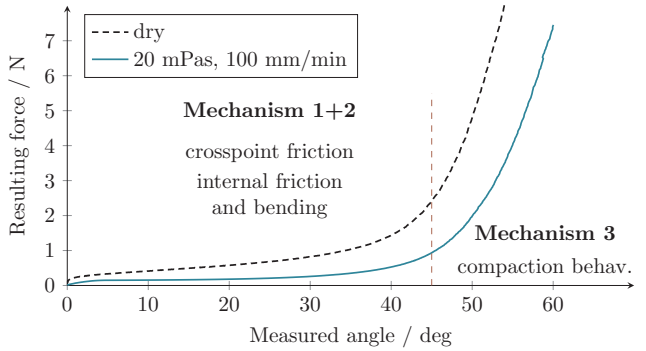

Fig. 9. Contribution of infiltration mechanisms (cf. Fig. 2) during IBETs. (For interpretation of the references to color in this figure legend, the reader is referred to the web version of this article.)

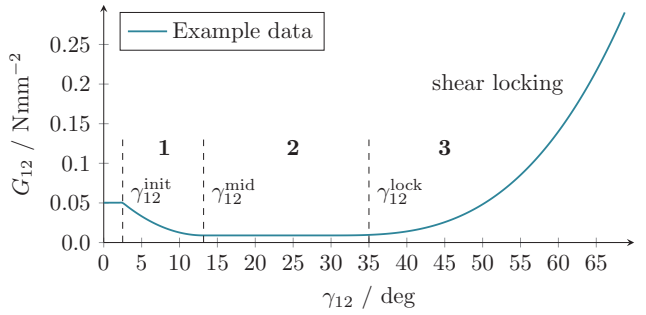

Fig. 10. Exemplary data for the implemented nonlinear shear modulus on initial configuration consisting of three piecewise functions with first order continuity. (For interpretation of the references to color in this figure legend, the reader is referred to the web version of this article.)

3.4. Discussion of the experimental results

Since mesoscopic effects (sliding and bending) occur when using the IBET set up, their impact on the locking angle is investigated by means of additional PF tests (Section 3.2). Results revealed that the IBET set up is a reliable and quick test method, well suited for infiltrated shear characterisations of a wide range of angles including an accurate pre diction of the locking angle. This is in accordance with the re commendations and findings in literature [14 16]. Thus, the impact of mesoscopic effect is found to be small below the locking angle and not noticeable effected by the infiltration. This holds true, even for

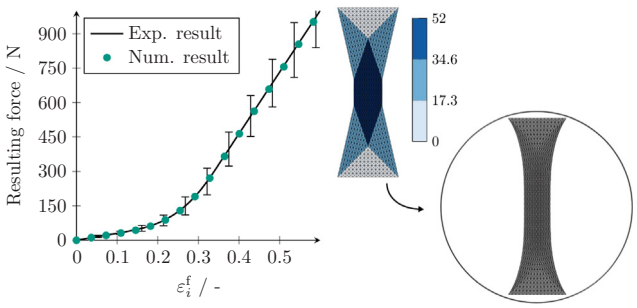

Fig. 11. Parametrisation results for uni-axial tension tests in fiber direction (left); Intermediate and final shape during BET simulations in Abaqus (right). (For interpretation of the references to color in this figure legend, the reader is referred to the web version of this article.)

relatively coarse woven fabrics (12 K) as investigated in this study, where the impact of mesoscopic effects is expected to by higher.

The experimental results reveal a rate and infiltration dependent material response of the infiltrated woven fabric. Shear resistance of the material can be reduced significantly by infiltration with low viscosity fluids (20 mPa s), even for the highest tested deformation rate (cf. Fig. 8). Beyond that, shear resistance of the material increases with viscosity and deformation rate and can reach values twice as high as the dry specimens (cf. Fig. 7 (detail (c))). In addition, differences in the characteristic of the infiltrated curves and a shift of the locking angle are found.

The experimental findings can be discussed in the context of the infiltration mechanisms outlined in Fig. 2 (see Section 3.2). The con tribution of the infiltration mechanism to the material shear response is shown in Fig. 9. At lower shear angles, shear resistance of the material is mostly determined by friction at the crosspoints. Since the infiltration reduces the friction coefficient at the crosspoints (mechanism 1) and reduces the bending stiffness of the rovings (mechanism 2), the shear resistance decreases and shows less increase compared to the dry curves. At higher shear angles, the change in compaction behaviour (mechanism 3) of the infiltrated rovings is expected to contribute to the shift of the locking angle, especially for low viscosity. This is reasonable since the outer contour and mesoscopic slip is measured to be constant and can therefore not be the reason for the shift.

To summarize, a significant impact of infiltration is found regarding shear behaviour of the tested plain weave woven fabric, including an additional rate and viscosity dependency. Beyond that, results are correlated with the expected infiltration mechanisms.

Table 1
Experimental determined material parameters.

	E_i^{init} N mm^{-2}	E_i^{end} N mm^{-2}	ε_i^{init} –	ε_i^{end} –	
dry	844.53	7248.36	$1.37e^{-3}$	$3.21e^{-3}$	
	k_1^{P1}	k_2^{P1}	k_3^{P1}	k_4^{P1}	
dry	$4.22e^{8}$	$1.15e^{6}$	$1.63e^{3}$	15.95	
	k_1^{P2}	k_2^{P2}	k_3^{P2}	k_4^{P2}	
dry	0.986	0.551	0.099	6.400	
20	0.846	0.390	0.052	4.565	
135	1.189	0.547	0.072	4.300	
250	1.634	0.844	0.123	4.427	
	G_1 N mm^{-2}	G_2 N mm^{-2}	γ_{12}^{init} rad	γ_{12}^{mid} rad	γ_{12}^{lock} rad
dry	0.097	0.023	0.005	0.280	0.545
20	0.039	0.007	0.036	0.231	0.571
135	0.050	0.009	0.044	0.230	0.558
250	0.084	0.014	0.053	0.258	0.550
	I_{12}^{v} s^{-1}	k_1^{P3} N mm^{-2}	k_2^{P3} N mm^{-2}	k_3^{P3} N mm^{-2}	k_4^{P3} N mm^{-2}
20	<0.05	0.002	0	0	0
	0.05–0.10	0.0215	1.461	1.666	0.496
	⩾ 0.10	0.0250	1.753	2.123	0.668
135	<0.05	0.002	0	0	0
	0.05–0.10	0.0204	1.648	1.714	0.467
	⩾ 0.10	0.0208	1.551	1.616	0.442
250	<0.05	0.002	0	0	0
	0.05–0.10	0.030	1.197	1.257	0.360
	⩾ 0.10	0.0281	1.237	1.302	0.371

4. Numerical model and investigations

To assess the process relevance of the findings in Section 3.3, a numerical study is conducted by means of FE forming simulations on a generic double dome geometry. The model is implemented in the commercially available FE solver Abaqus by means of two user sub routines for the user defined membrane behaviour (VUMAT) and the user defined bending behaviour (VUGENS) simular to [8]. First, a modelling approach for the membrane behaviour is presented and parametrised. Afterwards, effects on part level are investigated and evaluated.

4.1. Constitutive equations for membrane behaviour

The implemented hyperviscoelastic formulation is based on in variants of the Green Lagrange strain tensor $\boldsymbol{E}$ and the rate of de formation tensor $\boldsymbol{D}$. Two deformation modes, elongation in both fibre directions and shear, are taken into account and thus contribute to the potential of free energy Ψ given by

$$\Psi(I_1^e, I_2^e, I_{12}^e, I_{12}^v) = \Psi^{elong}(I_1^e, I_2^e) + \Psi^{shear}(I_{12}^e, I_{12}^v), \tag{2}$$

where I_1^e and I_2^e provide the elastic strain in the two fibre direction and $I_{12}^{e,v}$ the elastic, respectively viscous shear strain.

4.1.1. Elongation in fibre direction

The nonlinear hyperelastic elongation in fibre direction is modelled by means of elastic invariants of the Green Lagrange strain tensor $\boldsymbol{E} = \frac{1}{2}\cdot(\boldsymbol{F}^T\cdot\boldsymbol{F}-\boldsymbol{I})$,

$$\begin{aligned} I_1^e &= \boldsymbol{E}\colon(\boldsymbol{G_1}\otimes\ \boldsymbol{G_1}) = \varepsilon_1^e \\ I_2^e &= \boldsymbol{E}\colon(\boldsymbol{G_2}\otimes\ \boldsymbol{G_2}) = \varepsilon_2^e, \end{aligned} \tag{3}$$

where $\boldsymbol{G_1}$ and $\boldsymbol{G_2}$ provide the initial fibre orientations. The elastic components for the second Piola Kirchhoff tensor $\boldsymbol{S}$ are calculated using the invariants from Eq. (3) coupled with the nonlinear elastic moduli $E_1^f(I_1^e)$ and $E_2^f(I_2^e)$:

$$\begin{aligned} \boldsymbol{S}^e &= E_1^f(I_1^e)I_1^e(\boldsymbol{G_1}\otimes\ \boldsymbol{G_1}) = E_1^f(I_1^e)[\boldsymbol{E}\colon(\boldsymbol{G_1}\otimes\ \boldsymbol{G_1})](\boldsymbol{G_1}\otimes\ \boldsymbol{G_1}) \\ \boldsymbol{S}^e &= E_2^f(I_2^e)I_2^e(\boldsymbol{G_2}\otimes\ \boldsymbol{G_2}) = E_2^f(I_2^e)[\boldsymbol{E}\colon(\boldsymbol{G_2}\otimes\ \boldsymbol{G_2})](\boldsymbol{G_2}\otimes\ \boldsymbol{G_2}). \end{aligned} \tag{4}$$

Nonlinear fibre moduli E_1^f, E_2^f are implemented as functions of the corresponding directional invariants I_1^e and I_2^e using a second order polynomial (P1),

$$E_i^f(I_i^e) = \begin{cases} E_i^{init} & ;\ I_i^e \leqslant \varepsilon_i^{init} \\ k_1^{P1}\cdot I_i^2 + k_2^{P1}\cdot I_i^e + k_3^{P1} & ;\ \varepsilon_i^{init} < I_i^e \leqslant \varepsilon_i^{end}, \\ E_i^{end} + k_4^{P1}/I_i^e & ;\ I_i^e > \varepsilon_i^{end} \end{cases} \tag{5}$$

with the polynomial coefficients k_i^{P1}.

In general, Abaqus uses a polar decomposition of the deformation gradient into a symmetric stretch (deformation) tensors $\boldsymbol{U}$ and a non orthogonal rotation tensor $\boldsymbol{R}$, which defines a material fixed frame $(\hat{x}, \hat{y})$. This multiplicative decomposition is given by:

$$\boldsymbol{F} = \boldsymbol{R}\cdot\boldsymbol{U} \tag{6}$$

The second Piola Kirchhoff tensor $\boldsymbol{S}$ is transformed (pushed) to the material fixed frame $(\hat{x}, \hat{y})$ via the stretch tensor $\boldsymbol{U}$ by

$$\hat{\sigma} = \frac{1}{J}\cdot(\boldsymbol{U}\cdot\boldsymbol{S}\cdot\boldsymbol{U}), \tag{7}$$

where J provides the determinant of the deformation gradient $J = \det(\boldsymbol{F})$.

4.1.2. Shear behaviour

A nonlinear hyperviscoelastic shear behaviour is implemented by means of invariants of the Green Lagrange strain tensor $\boldsymbol{E}$ and the rate of deformation tensor $\boldsymbol{D}$:

$$\begin{aligned} I_{12}^e &= \tfrac{1}{2}[\boldsymbol{E}\colon(\boldsymbol{G_1}\otimes\ \boldsymbol{G_2}) + \boldsymbol{E}\colon(\boldsymbol{G_2}\otimes\ \boldsymbol{G_1})] \\ I_{12}^v &= \ \ [\boldsymbol{D}\colon(\boldsymbol{g_1}\otimes\ \boldsymbol{g_2}) + \boldsymbol{D}:(\boldsymbol{g_2}\otimes\ \boldsymbol{g_1})]. \end{aligned} \tag{8}$$

The rate of deformation tensor $\boldsymbol{D}$ is given by

$$\boldsymbol{D} = \frac{1}{2}(\dot{\boldsymbol{F}}\cdot\boldsymbol{F}^{-1} + \boldsymbol{F}^{-T}\cdot\dot{\boldsymbol{F}}^T), \tag{9}$$

with respect to current configuration $\{\boldsymbol{g_1}\otimes\ \boldsymbol{g_2}\}$.

The elastic shear components of the second Piola Kirchhoff tensor $\boldsymbol{S}$ are calculated by

$$\boldsymbol{S}^e = G_{12}(I_{12}^e)\cdot\frac{1}{2}I_{12}^e[(\boldsymbol{G_1}\otimes\ \boldsymbol{G_2}) + (\boldsymbol{G_2}\otimes\ \boldsymbol{G_1})], \tag{10}$$

where $G_{12}(I_{12}^e)$ provides a nonlinear shear modulus, which uses a third order polynomial (P2) to account for the shear locking. Moreover, a second order polynomial to account for the stiffness decrease between the initial and the constant mid section of the measured shear response (cf. Fig. 7)

$$G_{12}(I_{12}^e) = \begin{cases} G_1 & ;\ 0 \leqslant I_{12}^e \leqslant \gamma_{12}^{init} \\ k_1^{P2}\cdot I_{12}^2 + k_2^{P2}\cdot I_{12}^e + k_3^{P2} & ;\ \gamma_{12}^{init} < I_{12}^e \leqslant \gamma_{12}^{mid} \\ G_2 & ;\ \gamma_{12}^{mid} < I_{12}^e \leqslant \gamma_{12}^{lock} \\ k_4^{P2}\cdot(I_{12}^e - I_{12}^{e,lock})^3 + G_2 & ;\ I_{12}^e > \gamma_{12}^{lock}. \end{cases} \tag{11}$$

The polynomial coefficients k_i^{P2} are calculated with respect to $\mathscr{C}^1$ continuity between the regions 1 2 and 2 3 (Fig. 10).

The viscous shear components of the Kirchhoff stress tensor τ^v are given by

$$\tau^{v} = 2\eta(I_{12}^{e}, I_{12}^{v}) \cdot I_{12}^{v} [(\boldsymbol{g_1} \otimes \boldsymbol{g_2}) + (\boldsymbol{g_2} \otimes \boldsymbol{g_1})], \tag{12}$$

where $\eta(I_{12}^{e}, I_{12}^{v})$ provides a nonlinear viscosity according to

$$\eta(I_{12}^{e}, I_{12}^{v}) = \begin{cases} k_1^{P3}(I_{12}^{v}) & ; I_{12}^{e} \leqslant I_{12}^{lock} \\ k_2^{P3}(I_{12}^{v}) \cdot {I_{12}^{e}}^2 + k_3^{P3}(I_{12}^{v}) \cdot I_{12}^{e} + k_4^{P3}(I_{12}^{v}) & ; I_{12}^{e} > I_{12}^{lock}, \end{cases} \tag{13}$$

which accounts for the viscous part by means of another third order polynomial (P3) with rate dependent coefficients $k_i^{P3}(I_{12}^{v})$. The Kirchhoff stress tensor τ^{v} is transformed (pulled) to the initial configuration by means of the deformation gradient $\boldsymbol{F}$.

Finally, the elastic shear stress is superimposed to the viscous shear part according to an Voigt Kelvin approach by

$$\boldsymbol{S}(I_{12}^{e}, I_{12}^{v}) = \boldsymbol{S}^{e}(I_{12}^{e}) + \boldsymbol{S}^{v}(I_{12}^{v}) \tag{14}$$

and transformed (pushed) to the material fixed frame $(\hat{x}, \hat{y})$ used by Abaqus.

4.2. Parametrisation of the membrane model

Elongation in fibre direction. The experimental results of the uni axial BETs are used to parametrise the material behaviour in fibre direction. The results are illustrated in Fig. 11(a) and the identified parameters are presented in Table 1. The test set up is simulated in Abaqus to identify the material parameters.

Shear behaviour. A finite element simulation of the BET is conducted and the tested velocities from the experiments as boundary conditions.

The resulting force displacement curves are used to parametrise the model by comparison with the averaged test curves (cf. Fig. 12). Furthermore, the outer contour of the numerical sample is tracked and compared to experimental results (cf. Fig. 13). Parametrisation values are presented in Table 1. The numerical results are in good agreement with the experimental ones. Due to mesoscopic fibre slip, which cannot be taken into account with the macroscopic approach, test curves cannot be matched simultaneous for the outer contour and the force displacement curve for shear angles above 55 degrees. However, shear angles above 45 degrees did no arise within the numerical study on part level (cf. Section 4.3). To match the force displacement curves in combination with the specimen's outer contour using a macroscopic approach (cf. Fig. 13), either local parameters have to be assigned or homogenised fiber slippage mechanisms have to be taken into account.

4.3. Sensitivity analysis by means of forming simulation

The presented membrane model is used to evaluate the influence of infiltrated and rate dependent shear behaviour on part level by means of FE forming simulation for a generic double dome geometry. The shear rates, which result from the tool stroke amplitude during the forming simulation, are within the characterised range.

Forming simulation of woven single plies with initial fibre orientations of 0/90 and +45/−45 degrees are performed in Abaqus/Explicit. Explicit time integration is used due to large contact area between the ply and the tools. The tools are modelled as discrete rigid bodies and the tool stroke, which is implemented via a displacement boundary condition, corresponds to real process conditions. Since the double dome geometry is double symmetric, only one quarter is simulated with corresponding symmetry boundary conditions. Each ply is modelled by means of 49.600 triangular membrane and superimposed shell elements with suppressed membrane behaviour [8]. Bending behaviour is modelled with an orthotropic elastic stiffness of $B_i = 300\,\mathrm{N\,mm^{-2}}$ within a non orthogonal material frame. In this manner, the change of fibre orientation is accurately taken into account for arbitrary shear angles. The membrane part of the shell element is

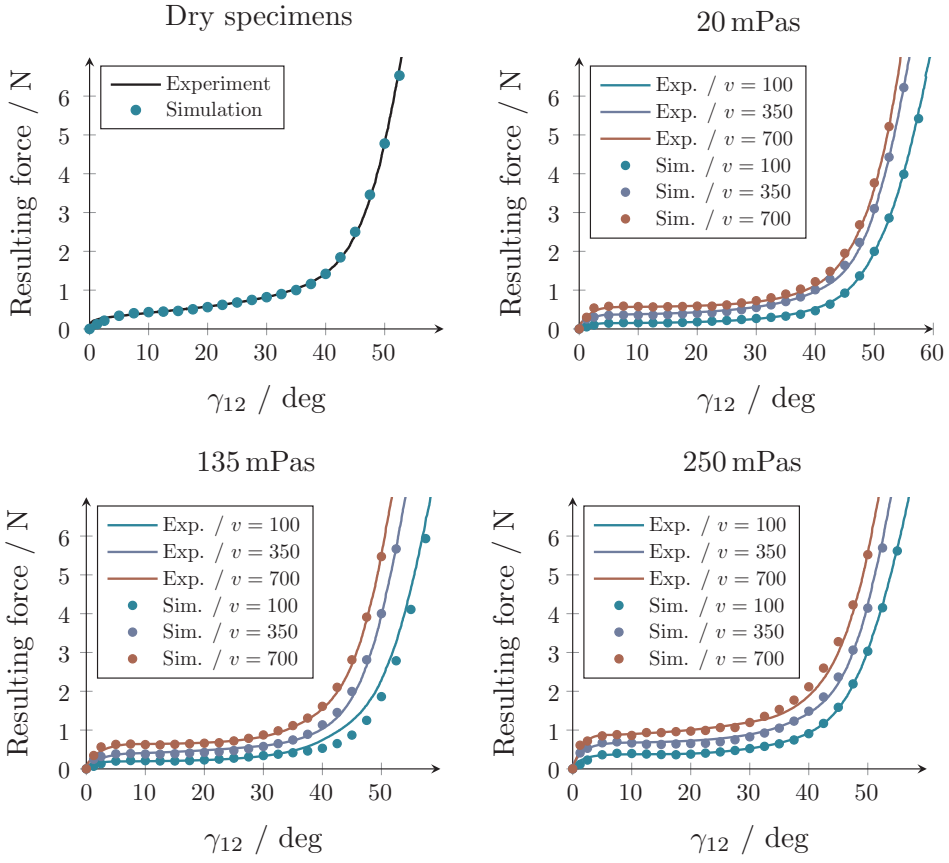

Fig. 12. Parametrisation results for the numerical BET, including dry and infiltrated specimens with varying velocity [mm s^{-1}]. (For interpretation of the references to color in this figure legend, the reader is referred to the web version of this article.)

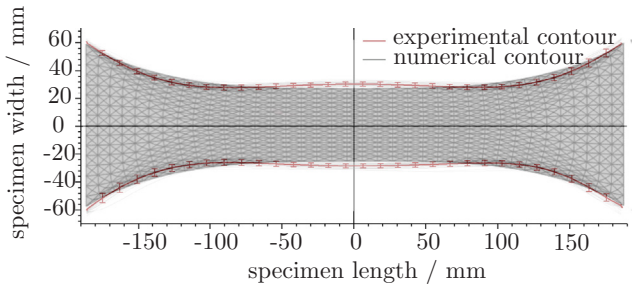

Fig. 13. Comparison of the experimental results of the optical contour evaluation and the numerical contour solution during bias-extension tests. (For interpretation of the references to color in this figure legend, the reader is referred to the web version of this article.)

suppressed by a user defined integration over the thickness of the shell element, which is implemented in a VUGENS subroutine. Tool ply contact is model via the built in general contact algorithm in Abaqus, using a friction coefficient of $\mu_{\text{ply-tool}} = 0.3$. FE forming simulations with parameter sets for dry and infiltrated specimens (dry, 20, 135, 250 mPa s (see Section 4.2)) for the membrane behaviour are carried out. Bending and contact behaviour is assumed to remain constant in the current study, to enable the isolated observation and evaluation of the shear mechanism.

4.4. Numerical results

Two zones of interest are selected and evaluated (major shear deformation zones) in comparative plots for both initial fibre orientations (cf. Fig. 14). The zones are evaluated in terms of the top 10 percent of the occurring shear angles with respect to the remaining tool stroke. Results for zone 1 (0/90) (cf. Fig. 14(a)) show, that the initial and final shear angles are in good agreement for all viscosities, but differences up to 9 degree arise during forming. In zone 2 (0/90) (cf.Fig. 14(b)), differences arise and remain even for the final fibre orientation (tool closed). Both zones are interconnected. While the results for the highest tested viscosity (250 mPa s) provide the lowest shear deformation in zone 1, it provides the highest in zone 2. Similar results are found the fibre orientation of $+45/-45$ (cf. Fig. 14(c, d)). However, no significant difference for the final fibre orientation can be found.

Furthermore, the global shear distribution is compared. Since differences arise mostly during forming, Fig. 15 provides exemplary field plots for the shear angle distribution with respect to different infiltration states (dry, 20, 135, 250 mPa s) for a remaining tool cavity of 4.5 mm. Despite the top 10 percent values, comparison of the results within this zones indicate that the shear distributions of dry and infiltrated fabrics with low viscosity (20 mPa s) are smoother than for the ones infiltrated with higher viscous fluids (250 mPa s). This is compatible with smoother distributions outside the zones 1 and 2 for infiltrated fabrics with low viscosity and sharper distributions for the ones infiltrated with higher viscous fluids. Similar results are found for the shear angle distribution within the highlighted region (a) of the completely closed tool (cf. Fig. 16). The predicted final shear angles in zone 1 (0/90) are identical for all viscosities.

4.5. Discussion of the numerical results

Numerical results on component level indicate an influence of the resin on to the shear deformation behaviour. As illustrated in Fig. 14(a–d), shear angle distributions are significantly effected during forming and effect each other within zones of interest, as well as on global scale (cf. Figs. 15 and 16).

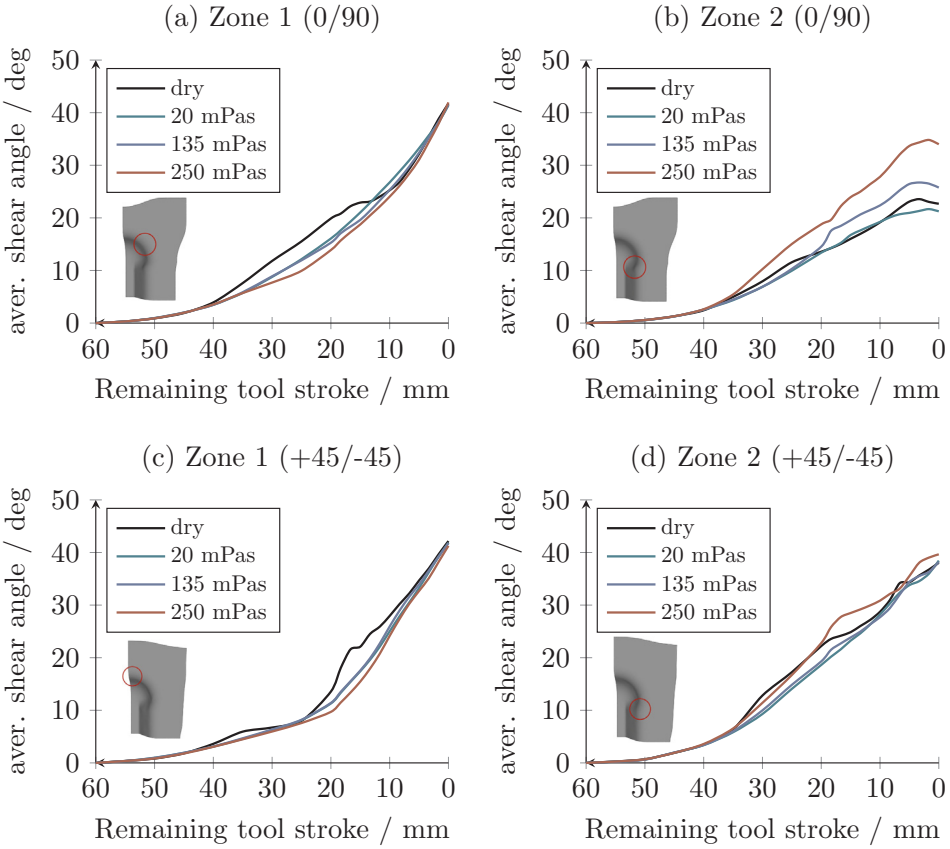

Fig. 14. Top 10% averaged shear angles of the 0/90, respectively +45/ 45 degree single ply during forming for Zone 1 and 2, including illustrations of the evaluated zones. (For interpretation of the references to color in this figure legend, the reader is referred to the web version of this article.)

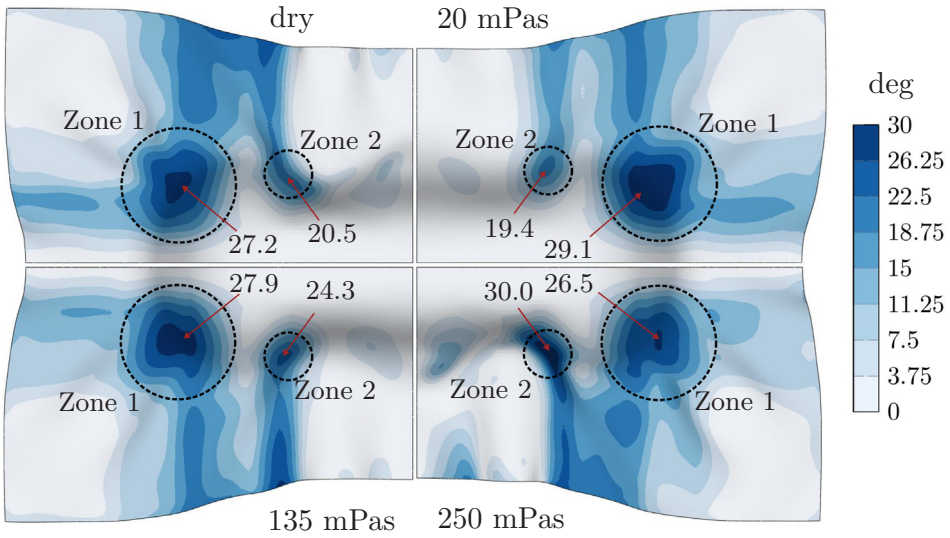

Fig. 15. Comparison of the shear angle distribution for a 0/90 woven fabric single ply with a remaining cavity of 4.5 mm, maxima in zone 1 and 2 are highlighted. (For interpretation of the references to color in this figure legend, the reader is referred to the web version of this article.)

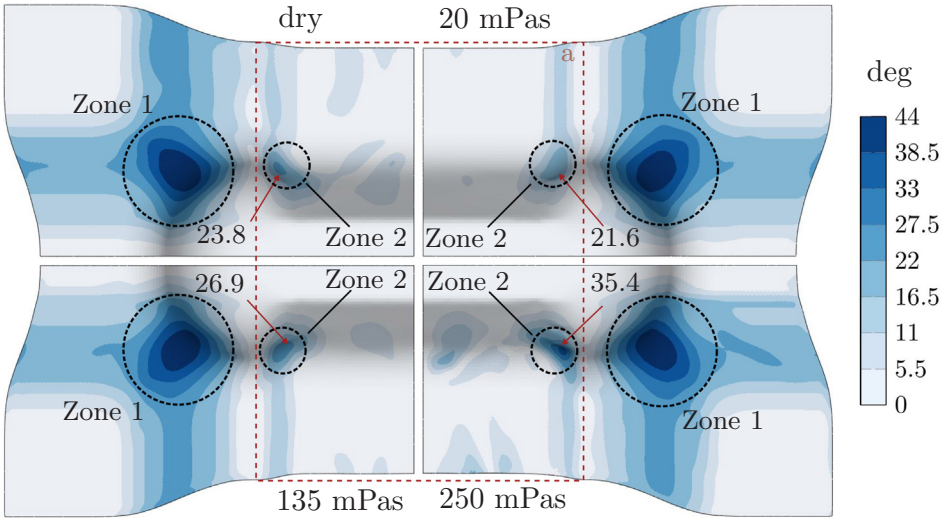

Fig. 16. Comparison of the shear angle distribution for a fully draped 0/90 woven fabric single ply; Zone 1 provides similar angles of 44 deg; Maxima in zone 2 are highlighted. (For interpretation of the references to color in this figure legend, the reader is referred to the web version of this article.)

Since no winkling occurs within the main deformation zone 1 (cf. Figs. 14(a, c) and 16), no differences can be observed for the final shear angle distribution in zone 1 for the investigated infiltration states. This is due to the kinematic constrains applied by the tool cavity, which remains constant. This only applies to rather simple geometries and might not be true in case of more complex geometries. The kinematic constrains are also the reason for the interconnection of the result in the zones 1 and 2.

Since shear resistance decreases for the fabrics infiltrated with low viscous fluids (20 mPa s), they tend to limit there deformation to the most need regions (good drapability), depending on the geometry. This leads to a very smooth deformation distribution. Thus, shear de formation in zone 1 increases, while the shear deformation in zone 2 decreases (cf. Fig. 15). On the contrary, infiltration with higher viscous fluids (250 mPa s) can decrease the drapability by localisation of shear deformation, which does not occur for dry or infiltrated fabrics with low viscous fluids (cf. Fig. 15). Beyond that, fabrics infiltrated with higher viscous fluids show more regions, where intensified shear de formation occurs (cf. Fig. 16).

However, some limitations have to be outlined. First, only the in plane behaviour is adapted to the infiltration and viscosity of the resin. This allows a decoupled investigation of this mechanism, but also limits the resilience of the results on part level, since infiltration will also influence bending and contact behaviour. Moreover, the results are limited to the investigated geometry, which means that tendencies derived in this section might not be confirmed for other geometries. Finally, an increasing viscosity due to curing and the coupling with resin propagation during forming is neglected in this study.

5. Conclusion

A modified test bench enabling shear characterisation of infiltrated engineering textiles is presented, validated and applied. The shear re sponse for three different viscosities and velocities of a plain weave woven fabric is investigated and compared to dry results. Both, rate and viscosity dependency is found during the experimental investiga tion. Possible infiltration mechanisms (change of friction on cross points, internal friction and compaction behaviour) are proposed to explain the different characteristics of the infiltrated shear curves compared to the dry ones.

Beyond that, the occurrence of mesoscopic effects during bias ex tension tests (fibre slip and bending) are discussed and their impact on

the results is estimated by means of additional picture frame tests. Results proved that the locking angle is predicted correctly for the modified infiltrated bias extension test, despite the mesoscopic effects. In addition, no measurable infiltration dependency of the discussed mesoscopic effects is found, since outer contour is found to be constant.

Furthermore, a parametrised membrane model is presented and applied to access and estimate the process relevance of the identified infiltrated material response by means of FE forming simulation for a generic geometry. Numerical results indicate an important impact of the infiltration on the shear angle distribution during draping.

Future work will scope on proper consideration of infiltration de pendent material models for bending and contact behaviour to achieve a comprehensive understanding of the infiltrated draping. Moreover, the prediction of simultaneous fluid propagation during draping is a major objective of future research. This includes the implementation of fluid propagation and of mutual dependencies between infiltrated forming and fluid propagation to enable a physical based process si mulation modelling.

Acknowledgment

The authors would like to thank the German State Ministry for Science, Research and Art of Baden Württemberg (MWK) for the funding of the project Forschungsbrücke Karlsruhe Stuttgart for which the presented work is carried out. The work is also part of the Young Investigator Group (YIG) “Tailored Composite Materials for Lightweight Vehicles”, funded by the Vector Stiftung.

References

[1] Bergmann J, Dörmann H, Lange R. Interpreting process data of wet pressing process. Part 1: Theoretical approach. J Compos Mater 2016;50(17):2399–407. https://doi.org/10.1177/0021998315604728.

[2] Bergmann J, Dörmann H, Lange R. Interpreting process data of wet pressing process. Part 2: Verification with real values. J Compos Mater 2016;50(17):2409–19. https://doi.org/10.1177/0021998315604038.

[3] Bockelmann P. Process control in compression molding of composites [Dissatationen]. München: Fakultät für Maschinenwesen, Technische Universität; 2017.

[4] Heudorfer, Carosella, Middendorf. Compression wet moulding as alternative to RTM, 25. Stuttgarter Kunststoffkolloquium, 22./23. März; 2017.

[5] Poppe C, Dörr D, Henning F, Kärger L. A 2D modeling approach for fluid propagation during finite element forming simulation of continuously reinforced composites in wet compression moulding. In: AIP conference proceedings; 2018. https://doi.org/10.1063/1.5034823.

[6] Machado M, Fischlschweiger M, Major Z. A rate-dependent non-orthogonal constitutive model for describing shear behaviour of woven reinforced thermoplastic composites. Compos Part A: Appl Sci Manuf 2016;80:194–203.

[7] Boisse P, Hamila N, Guzman-Maldonado E, Madeo A, Hivet G, Dell’Isola F. The bias-extension test for the analysis of in-plane shear properties of textile composite reinforcements and prepregs: a review. Int J Mater Form 2016;78(5):26.

[8] Dörr D, Schirmaier FJ, Henning F, Kärger L. A viscoelastic approach for modeling bending behavior in finite element forming simulation of continuously fiber reinforced composites. Compos Part A: Appl Sci Manuf 2017;94:113–23. https://doi.org/10.1016/j.compositesa.2016.11.027.

[9] Cao J, Akkerman R, et al. Characterization of mechanical behavior of woven fabrics: experimental methods and benchmark results. Compos Part A: Appl Sci Manuf 2008;39(6):1037–53. https://doi.org/10.1016/j.compositesa.2008.02.016.

[10] Schirmaier FJ, Weidenmann KA, Kärger L, Henning F. Characterisation of the draping behaviour of unidirectional non-crimp fabrics (ud-ncf). Compos Part A: Appl Sci Manuf 2016;80:28–38. https://doi.org/10.1016/j.compositesa.2015.10.004.

[11] Boisse P, Hamila N, Vidal-Sallé E, Dumont F. Simulation of wrinkling during textile composite reinforcement forming. Influence of tensile, in-plane shear and bending stiffnesses. Compos Sci Technol 2011;71(5):683–92. https://doi.org/10.1016/j.compscitech.2011.01.011.

[12] Willems A. Forming simulations of textile reinforced composite shell structures [Dissertation]. Herverlee, Belgium: Katholieke Universiteit Leuven; 2008.

[13] Colman AG, Bridgens BN, Gosling PD, Jou G-T, Hsu X-Y. Shear behaviour of architectural fabrics subjected to biaxial tensile loads. Compos Part A: Appl Sci Manuf 2014;66:163–74. https://doi.org/10.1016/j.compositesa.2014.07.015.

[14] Harrison P, Clifford MJ, Long AC. Shear characterisation of viscous woven textile composites: a comparison between picture frame and bias extension experiments. Compos Sci Technol 2004;64(10–11):1453–65. https://doi.org/10.1016/j.compscitech.2003.10.015.

[15] Zhu B, YU T, TAO X. Large deformation and slippage mechanism of plain woven composite in bias extension. Compos Sci Technol 2007;38(8):1821–8. https://doi.org/10.1016/j.compscitech.2007.04.009.

[16] Bel S, Boisse P, Dumont F. Analyses of the deformation mechanisms of non-crimp fabric composite reinforcements during preforming. Appl Compos Mater 2012;19(3–4):513–28. https://doi.org/10.1007/s10443-011-9207-x.

[17] Nosrat-Nezami F, Gereke T, Eberdt C, Cherif C. Characterisation of the shear–tension coupling of carbon-fibre fabric under controlled membrane tensions for precise simulative predictions of industrial preforming processes. Compos Part A: Appl Sci Manuf 2014;67:131–9. https://doi.org/10.1016/j.compositesa.2014.08.030.

[18] Galliot C, Luchsinger RH. The shear ramp: a new test method for the investigation of coated fabric shear behaviour – part i: Theory. Compos Part A: Appl Sci Manuf 2010;41(12):1743–9.

[19] Kashani MH, Rashidi A, Crawford BJ, Milani AS. Analysis of a two-way tension-shear coupling in woven fabrics under combined loading tests: global to local transformation of non-orthogonal normalized forces and displacements. Compos Part A: Appl Sci Manuf 2016;88:272–85. https://doi.org/10.1016/j.compositesa.2016.06.004.

[20] Haanappel SP, ten Thije R, Sachs U, Rietman B, Akkerman R. Formability analyses of uni-directional and textile reinforced thermoplastics. Compos Part A: Appl Sci Manuf 2014;56:80–92. https://doi.org/10.1016/j.compositesa.2013.09.009.

[21] Guzman-Maldonado E, Hamila N, Naouar N, Moulin G, Boisse P. Simulation of thermoplastic prepreg thermoforming based on a visco-hyperelastic model and a thermal homogenization. Mater Des 2016;93:431–42. https://doi.org/10.1016/j.matdes.2015.12.166.

[22] Dörr D, Henning F, Kärger L. Nonlinear hyperviscoelastic modelling of intra-ply deformation behaviour in finite element forming simulation of continuously fibre-reinforced thermoplastics. Compos Part A: Appl Sci Manuf 2018;109:585–96.

[23] Dörr D, Joppich T, Schirmaier F, Mosthaf T, Kärger L, Henning F. A method for validation of finite element forming simulation on basis of a pointwise comparison of distance and curvature. In: AIP conference proceedings; 2016. p. 170011. https://doi.org/10.1063/1.4963567.

[24] Soulat Damien, Cheruet Anthony, Boisse Philippe. Simulation of continuous fibre reinforced thermoplastic forming using a shell finite element with transverse stress. Comput Struct 2006:888–903. https://doi.org/10.1016/j.compstruc.2006.02.011.

[25] Denis Y, Guzman-Maldonado E, Hamila N, Colmars J, Morestin F. A dissipative constitutive model for woven composite fabric under large strain. Compos Part A: Appl Sci Manuf 2018;105:165–79. https://doi.org/10.1016/j.compositesa.2017.11.018.

[26] Boisse P, Naouar N, Charmetant A. Finite element analysis of composite forming at macroscopic and mesoscopic scale. In: Boisse P, editor. Advances in composites manufacturing and process design. Woodhead publishing series in composites science and engineering. Cambridge (UK): Woodhead Publishing; 2015. p. 297–315. https://doi.org/10.1016/B978-1-78242-307-2.00014-2.

[27] Boisse P, Hamila N, Madeo A. The difficulties in modeling the mechanical behavior of textile composite reinforcements with standard continuum mechanics of cauchy. Some possible remedies. Int J Solids Struct. https://doi.org/10.1016/j.ijsolstr.2016.12.019.

[28] Peng X, Guo Z, Du T, Yu W-R. A simple anisotropic hyperelastic constitutive model for textile fabrics with application to forming simulation. Compos Part B: Eng 2013;52:275–81. https://doi.org/10.1016/j.compositesb.2013.04.014.

[29] Komeili M, Milani AS. On effect of shear-tension coupling in forming simulation of woven fabric reinforcements. Compos Part B: Eng 2016;99:17–29. https://doi.org/10.1016/j.compositesb.2016.05.004.

[30] Eberl C, Bundschuh S. Digital image correlation and tracking: calculate displacement and strain from a series of images; 2010.